



# Pulsed Laser Annealed Ga Hyperdoped Poly-Si/SiO<sub>x</sub> Passivating Contacts for High-Efficiency Monocrystalline Si Solar Cells


Kejun Chen\* , Enrico Napolitani\* , Matteo De Tullio, Chun-Sheng Jiang, Harvey Guthrey, Francesco Sgarbossa, San Theingi, William Nemeth, Matthew Page, Paul Stradins, Sumit Agarwal, and David L. Young

**Polycrystalline Si (poly-Si)-based passivating contacts are promising candidates for high-efficiency crystalline Si solar cells. We show that nanosecond-scale pulsed laser melting (PLM) is an industrially viable technique to fabricate such contacts with precisely controlled dopant concentration profiles that exceed the solid solubility limit. We demonstrate that conventionally doped, hole-selective poly-Si/SiO<sub>x</sub> contacts that provide poor surface passivation of c-Si can be replaced with Ga- or B-doped contacts based on non-equilibrium doping. We overcome the solid solubility limit for both dopants in poly-Si by rapid cooling and recrystallization over a timescale of ~25 ns. We show an active Ga dopant concentration of  $\sim 3 \times 10^{20} \text{ cm}^{-3}$  in poly-Si which is six times higher than its solubility limit in c-Si, and a B dopant concentration as high as  $\sim 10^{21} \text{ cm}^{-3}$ . We measure an implied open-circuit voltage of 735 mV for Ga-doped poly-Si/SiO<sub>x</sub> contacts on Czochralski Si with a low contact resistivity of  $35.5 \pm 2.4 \text{ m}\Omega \text{ cm}^2$ . Scanning spreading resistance microscopy and Kelvin probe force microscopy show large diffusion and drift current in the p-n junction that contributes to the low contact resistivity. Our results suggest that PLM can be extended for hyperdoping of other semiconductors with low solubility atoms to enable high-efficiency devices.**

## 1. Introduction

The continuous improvement in efficiency and cost of monocrystalline Si (c-Si) solar cells requires devices with fully passivating contacts<sup>[1]</sup> that

K. Chen, Prof. S. Agarwal  
Colorado School of Mines, 1500 Illinois St, Golden Colorado 80401, USA  
E-mail: kejunchen@mines.edu  
Prof. E. Napolitani, M. D. Tullio, Dr. F. Sgarbossa  
Dipartimento di Fisica e Astronomia and CNR-IMM, Università degli Studi di Padova, via Marzolo 8, Padova, Italy  
E-mail: enrico.napolitani@unipd.it  
Dr. C.-S. Jiang, Dr. H. Guthrey, S. Theingi, W. Nemeth, M. Page,  
Dr. P. Stradins, Dr. D. L. Young  
National Renewable Energy Laboratory, 15013 Denver West Parkway, Golden Colorado 80401, USA

 The ORCID identification number(s) for the author(s) of this article can be found under <https://doi.org/10.1002/eam2.12542>.

DOI: 10.1002/eam2.12542

can replace the passivated-emitter and rear cell (PERC) architectures.<sup>[2–4]</sup> Passivating contacts based on the heavily doped polycrystalline Si (poly-Si) and an ultrathin interfacial SiO<sub>x</sub> are one of the most promising candidates for next-generation, high-efficiency c-Si solar cells.<sup>[5]</sup> In these contacts, the SiO<sub>x</sub> layer provides tunneling transport as well as chemical passivation by preventing recombination loss that would otherwise occur at the metal-to-semiconductor interface,<sup>[6]</sup> and the heavily doped poly-Si provides field-effect passivation.<sup>[7]</sup> Recently, laboratory-scale efficiency of solar cells with poly-Si/SiO<sub>x</sub> contacts have reached 26% for contacts based on <2 nm SiO<sub>x</sub>,<sup>[8,9]</sup> which are referred to as tunnel oxide passivating contacts (TOPCon).<sup>[10,11]</sup> Many industrially manufactured n-type c-Si solar cells with poly-Si/SiO<sub>x</sub> passivating contacts have demonstrated efficiencies >23%,<sup>[12–14]</sup> with a recent record cell of 26.1% efficiency.<sup>[15]</sup> These cells feature a phosphorus-doped (P-doped) poly-Si/SiO<sub>x</sub> passivating contact at the rear, and a front boron-diffused emitter. It is, however, of interest to apply the passivating contacts on both sides of

the cells to further improve the overall passivation, since the recombination on the front boron-diffused surface is responsible for the largest power loss in TOPCon cells.<sup>[16–18]</sup>

Phosphorus-doped poly-Si/SiO<sub>x</sub> contacts show a very high implied open-circuit voltage ( $iV_{oc}$ ) of >730 mV, with a very low dark saturation current density ( $J_0$ ) below  $1 \text{ fA cm}^{-2}$ .<sup>[19–21]</sup> Conversely, boron-doped (B-doped) poly-Si contacts have a lower  $iV_{oc}$  of ~710 mV with a  $J_0$  value of  $\sim 10 \text{ fA cm}^{-2}$ .<sup>[6,22]</sup> This phenomenon of inferior boron-doped contacts was previously observed in the bipolar junction and field-effect transistors in the 1990s.<sup>[23,24]</sup> Several studies have attributed it to the tendency of B to segregate at the interface between SiO<sub>x</sub> and c-Si,<sup>[25–30]</sup> increasing the density of interface defects.<sup>[27,31]</sup> We have previously shown that Ga can be used as an alternate p-type dopant in poly-Si and demonstrated high  $iV_{oc} > 730 \text{ mV}$  on symmetric p-type poly-Si/SiO<sub>x</sub>/n-type CZ c-Si test structures.<sup>[32]</sup> This improvement in passivation quality with Ga compared with B is attributed to a higher diffusivity of Ga in SiO<sub>x</sub>,  $D_{Ga}$ , which is almost six orders of magnitude higher than the diffusion coefficient of B in SiO<sub>x</sub>.<sup>[33,34]</sup> Compared with B, Ga also

has a nearly three orders of magnitude higher segregation coefficient in Si versus  $\text{SiO}_x$  ( $k_{\text{Ga}} \sim 20$  and  $k_{\text{B}} \sim 10^{-2}$ ),<sup>[35]</sup> which combined with the higher diffusivity prevents accumulation of Ga in  $\text{SiO}_x$  and at the  $\text{SiO}_x$ /*c*-Si interface. While the  $iV_{\text{oc}}$  for the Ga-doped contact in Young et al.<sup>[32]</sup> was better than B-doped contacts, the higher contact resistivity limits the fill factor after various annealing methods, ranging from 850 °C for 30 min to 950 °C for 1 s. It was determined that not enough Ga dopants were activated under these annealing conditions. Thus, in order to activate enough Ga in *poly*-Si to have a low contact resistivity to the metal contacts, non-equilibrium doping above the solubility limit (hyperdoping) needs to be introduced.

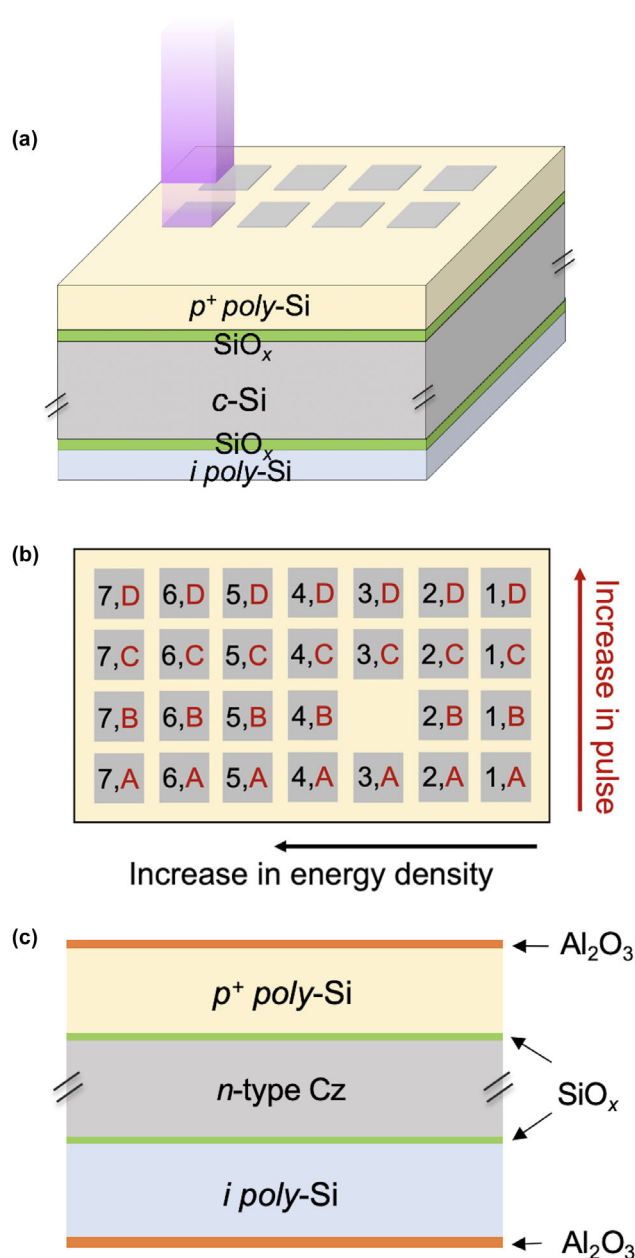
The maximum solid solubility limit of Ga in monocrystalline Si has been reported as  $4 \times 10^{19} \text{ cm}^{-3}$  at 1200 °C by Trumbore in 1959,<sup>[36]</sup> and the solid solubility limit is often lower (for example,  $1 \times 10^{19} \text{ cm}^{-3}$  at common cell processing temperatures of  $\sim 900 \text{ °C}$ )<sup>[37]</sup>. However, doping concentrations  $>10^{20} \text{ cm}^{-3}$  are desired for various applications, such as shallow  $p^+$  junction,<sup>[38,39]</sup> superconducting semiconductors,<sup>[40–42]</sup> and low contact resistivity *p*-type contacts for solar cells.<sup>[32,43]</sup> Conventional thermal processes cannot reach a high level of doping concentration, so to overcome the equilibrium solid solubility limit, some early studies in the 1980s based on non-equilibrium processes have shown supersaturated Ga in silicon with a substitutional doping level of  $1\text{--}8 \times 10^{20} \text{ cm}^{-3}$ <sup>[44–48]</sup> as well as an active doping concentration of  $\sim 3.5 \times 10^{20} \text{ cm}^{-3}$ .<sup>[49,50]</sup> But in all works reported, Ga was solely studied in single crystalline silicon, and no studies have been shown to investigate Ga hyperdoping in *poly*-Si or in *poly*-Si/ $\text{SiO}_x$  passivating contact structures.

This work explores Ga and B doping of *poly*-Si using an excimer laser with ns pulse duration (Figure 1a), rather than relying on the traditional furnace anneal (shown previously in Young et al.<sup>[32]</sup>). The essence of this approach is to take advantage of the nonequilibrium nature of the anneal by utilizing the short timescale and to achieve doping concentration above the solid solubility limit. The rapid melting of the *poly*-Si increases the diffusion coefficient of dopants and upon the removal of the laser pulse, the temperature of the *poly*-Si drops rapidly, and the molten *poly*-Si recrystallizes back. During this process, dopants are incorporated into the Si lattice at very high concentrations due to the extremely fast regrowth rate ( $>1 \text{ m s}^{-1}$ ), which leads to nonequilibrium doping.<sup>[51]</sup> We show the effect of laser energy density (ED) and number of pulses (Figure 1b) on the passivation quality of the sample (see structure in Figure 1c), as well as the transport and electrical behavior. These insights are significant and lead to improvements over boron-doped *p*-type *poly*-Si/ $\text{SiO}_x$  passivating contacts.

## 2. Results and Discussion

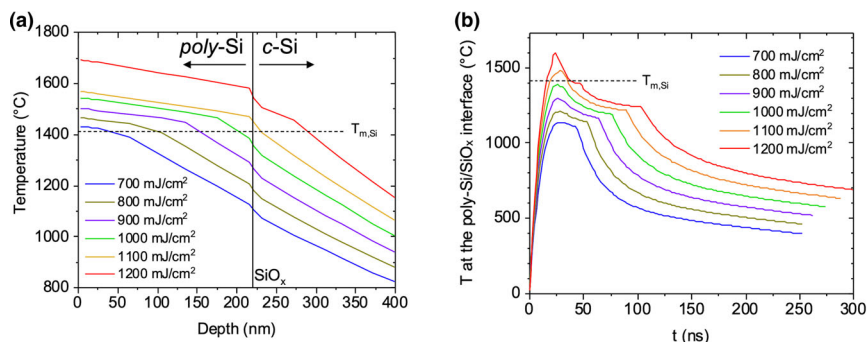
### 2.1. Simulation of Melt Depth and the Temperature of the $\text{SiO}_x$ /*c*-Si Interface

Figure 2a shows the simulated temperature–depth profiles for different laser EDs, from 700 to  $1200 \text{ mJ cm}^{-2}$ . For each ED, the temperature profile corresponds to the instant when the maximum melt depth is reached, which also provides the maximum temperature. Since the maximum melt depth can continue to increase even after the end of the pulse due to heat conduction, the simulated time for reaching the maximum melt depth for all the EDs investigated was  $\sim 25 \text{ ns}$  rather than 22 ns laser pulse length. The near-surface region of each profile shows a lower temperature gradient, followed by a higher temperature



**Figure 1.** a) Schematic of the sample with 250 nm of Ga- or 270 nm of B-doped *poly*-Si on  $\sim 1.5 \text{ nm}$   $\text{SiO}_x$  on top of *n*-type *c*-Si. On each  $30 \times 50 \text{ mm}^2$  sample, twenty-seven  $5.1 \times 5.1 \text{ mm}^2$  spots were processed with a KrF excimer laser with a wavelength of 248 nm. The laser beam is indicated in purple. b) Top view of the test structure in a). The numbers 1 to 7 represent seven different energy densities over the range of 300–1100  $\text{mJ cm}^{-2}$  for each laser pulse. The letters A–D represent the number of pulses at each energy density ranging from 1 to 6. One spot was not annealed for reference measurement of the pre-annealed state (3, B). c) Cross-sectional image of the non-symmetrical test structure after laser processing, passivated by depositing  $\text{Al}_2\text{O}_3$  on both sides.

gradient further away from the surface into the wafer. These two regions correspond to the liquid phase (molten *poly*-Si) and crystalline phase (solid *poly*-Si) of Si, respectively. The difference in the two temperature gradients is due to the higher thermal conductivity of the



**Figure 2.** a) Simulated temperature profile as a function of depth extracted at the times where the maximum melt depth is reached, in the *poly-Si/SiO<sub>x</sub>/c-Si* stack for various laser energy densities. This time is, for each ED, close to 25 ns. The *poly-Si* and *c-Si* regions are indicated at the top. The position of the  $\sim 1.5$  nm  $\text{SiO}_x$  layer is indicated by the vertical solid line. b) Temporal evolution of the simulated temperature at the *poly-Si/SiO<sub>x</sub>* interface for various laser energy densities. The dashed horizontal lines in a, b) show the melting temperature for *c-Si*,  $T_{m,\text{Si}}$ .

liquid phase with respect to the crystalline phase. The kink separating the two phases corresponds to the liquid–solid interface at the maximum melt depth, and its depth increases for increasing ED. Furthermore, the solid-to-liquid transition occurs in most cases at a temperature slightly higher than the melting temperature of Si,  $T_m = 1414$  °C, due to the solid superheating.<sup>[52]</sup> The figure clearly shows that high-temperature gradients are reached within the *poly-Si* solid phase up to 150 °C per 100 nm, due to the short absorption depth of  $\sim 5$  nm for the 248 nm laser wavelength and the short duration of the pulse. This feature is the basis of the method used in this work, as it allows to heat a shallow layer in *poly-Si* while preserving the chemical passivation of the  $\text{SiO}_x$  layer at the *poly-Si/SiO<sub>x</sub>* interface.

In Figure 2b, we report the simulated temperature at the *poly-Si/SiO<sub>x</sub>* interface as a function of time. In all cases, the temperature at the *poly-Si/SiO<sub>x</sub>* interface increases rapidly within the first 22 ns, remains high for only a very short duration, and then decreases slowly after the end of the short laser pulse. The temporal variation in temperature at the *poly-Si/SiO<sub>x</sub>* interface shows a strong dependence on the laser ED. For higher laser EDs, 1100 and 1200  $\text{mJ cm}^{-2}$ , the peak temperature exceeds the melting point of Si. For lower EDs, the temperature remained below  $T_{m,\text{Si}}$ . Therefore, we can conclude that a laser ED of less than 1000  $\text{mJ cm}^{-2}$  is necessary to not compromise the interfacial  $\text{SiO}_x$  layer, thus preserving the passivation quality after laser processing.

## 2.2. Dopant Diffusion and Activation

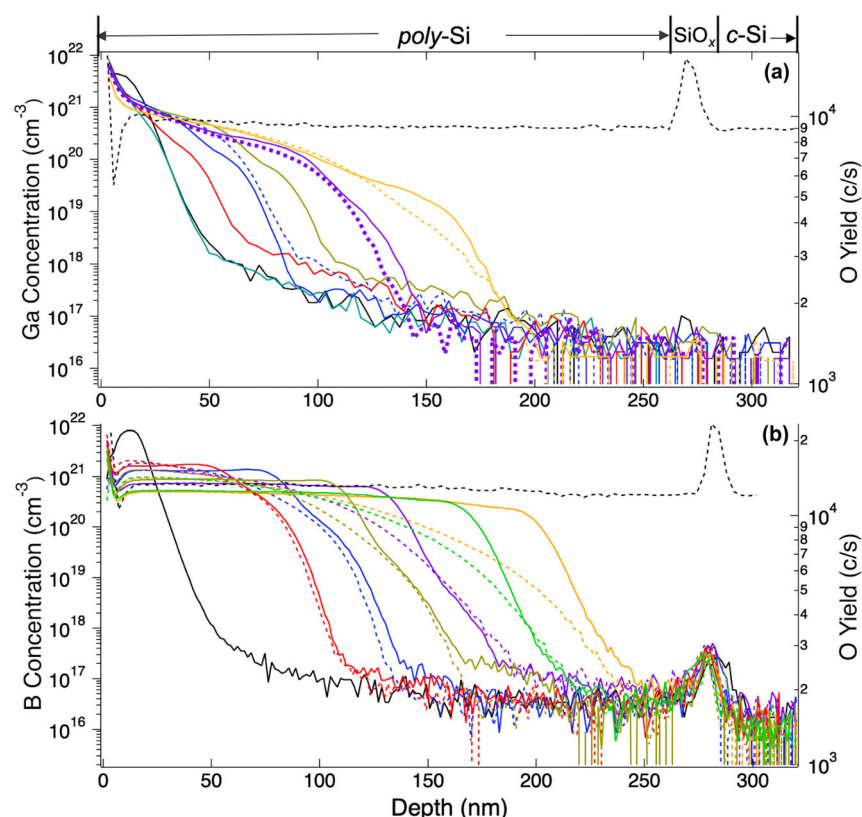
To visualize the dopant distribution profiles, secondary ion mass spectrometry (SIMS) measurements were performed on both Ga-implanted and B-doped via plasma enhance vapor deposition (PECVD) polished *c-Si* samples. Figure 3 shows the Ga and B concentration depth profiles for various laser EDs with 1 or 4 pulses. For comparison, we also show the depth profiles measured in unannealed regions. The profiles show a pronounced peak within the top 10–15 nm, which is an artifact and, in the case of B, also a small dip. Other artifacts include extended profile tails at low concentrations ( $< 5 \times 10^{17} \text{ cm}^{-3}$  for B, and  $< 10^{18} \text{ cm}^{-3}$  for Ga), and a background signal of  $\sim 3 \times 10^{16} \text{ cm}^{-3}$  for both dopants. Thus, SIMS can slightly overestimate the real dopant concentrations due to the background.

Figure 3a,b shows common diffusion features for both dopants after PLM: a) Diffusion of Ga and B occurs into the intrinsic *poly-Si* region at concentrations well above the solid solubility limit in *c-Si* ( $\sim 4 \times 10^{19} \text{ cm}^{-3}$  at 1200 °C for Ga, and  $\sim 5 \times 10^{20} \text{ cm}^{-3}$  at 1200 °C for B<sup>[36]</sup>); b) all depth profiles show a sharp decrease in concentration at depths ranging between 50 and 250 nm (as the dopants reach the maximum melt depth, the dopant diffusivity in the solid phase is orders of magnitude lower than in the liquid phase, which prevents profile broadening); and c) an increase in ED redistributes the dopants much deeper into the *poly-Si* due to the increase in the maximum melt depth, which is in qualitative agreement with the simulation shown in Figure 2a. In Figure 3b, as B penetrates deeper into *poly-Si*, the concentration in the surface region decreases as the dopant areal density is conserved during the PLM process. However, this effect is

much less pronounced for Ga. Both the Ga and B profiles do not reach the tunneling  $\text{SiO}_x$  layer, which is consistent with the simulation plot in Figure 2a. Yet, Figure 3a,b show a quite different diffusion behavior for Ga than for B. In the concentration profiles for B near the surface in Figure 3b, there are no clear signs of surface segregation, or out-diffusion. Therefore, with an increase in the number of pulses, which increases the time for diffusion, B redistributes further into “box-like” profiles. The diffusion behavior of B aligns well with the simulated diffusion depths at various EDs as shown in Figure 2a. To verify the B depth profile obtained from SIMS, we performed electron energy loss spectroscopy (EELS) measurements using high-angle annular dark field (HAADF) to obtain an elemental map for Si, O, and B. Figure 4a shows the cross-section HAADF image of a B-doped *poly-Si/SiO<sub>x</sub>* contact, and the EELS elemental mapping was performed in the region boxed in red. The Si and O elemental maps in Figure 4b,c, respectively, show that the  $\text{SiO}_x$  layer between *poly-Si* and *c-Si* is intact after PLM. The B map in Figure 4d was averaged across the width of the image boxed in red in Figure 4a, and a line plot was generated based on the pixel intensity. Figure 4e shows that the shape of the EELS depth profile for B matches well with that obtained from SIMS, which further confirms that the B atoms do not significantly penetrate in the *c-Si* bulk after PLM.

Contrary to B, in the case of Ga, the diffusion profiles are much shallower and exhibit a less sharp dopant drop off at the maximum melt depth. Additionally, the number of laser pulses does not seem to have a large effect on the doping behavior. This can be attributed to the difference in equilibrium segregation coefficients for Ga and B defined as  $k_{\text{eq}} = C_S/C_L$ , where  $C_S$  and  $C_L$  are the concentration of the dopant in the solid and the liquid phase, respectively. B has a  $k_{\text{eq}} = 0.8$ , which is two orders of magnitude higher than Ga,  $k_{\text{eq}} = 0.008$ .<sup>[36,53]</sup> Therefore, during the recrystallization process, B is more likely to incorporate in the crystalline *poly-Si*, whereas Ga tends to be pushed towards the surface with the molten front: this explains the gradual decrease in the Ga doping concentration profile moving deeper into the film in Figure 3a.

The O concentration depth profiles for the Ga and B doped samples are shown at the top in Figure 3a,b, which can be used to identify the  $\text{SiO}_x$  layer. The dopant profiles for Ga and B behave very differently in the  $\text{SiO}_x$  layer: B appears to pile up in the  $\text{SiO}_x$  layer, while Ga does not show any pileup. Indeed, this B concentration peak at the oxide is likely due to an oxygen matrix effect in SIMS,<sup>[54]</sup> as the witness unannealed



**Figure 3.** SIMS depth profile for a) Ga- and b) B-doped *poly-Si* samples for different laser energy densities and number of pulses. The six energy densities were 500 (—), 600 (—), 700 (—), 800 (—), 900 (—), 1000 (—), and 1100 (—)  $\text{mJ cm}^{-2}$ . Note the 500 and 1000  $\text{mJ cm}^{-2}$  conditions were not performed on B and Ga samples, respectively. For each energy density in a,b), the dashed, colored lines indicate 1 laser pulse, and the solid, colored lines indicate 4 laser pulses. The black solid line shows the dopant profile in an unprocessed region. The dashed black line at the top corresponds to the O yield in c/s shown on the right y-axis. The high apparent O background is due to  $\text{O}_2^+$  primary beam used for the SIMS analyses. The respective locations of *poly-Si*,  $\text{SiO}_x$ , and *c-Si* are shown at the top of the graphs.

region in Figure 3b also shows a higher concentration of B in the  $\text{SiO}_x$  layer. Thus, we can conclude that no accumulation of Ga or B in the  $\text{SiO}_x$  layer occurs due to PLM.

To gain insights into the electrical behavior of the Ga and B doped regions, Van der Pauw – Hall (VdP-Hall) measurements were performed in each laser annealed spot separately with the four probes directly contacting the four corners of the laser annealed region. Figure 5 shows the sheet resistance, and the hole Hall areal density for Ga (Figure 5a,b) and B (Figure 5c,d) for different laser EDs and numbers of pulses. We see for both Ga and B that the sheet resistance decreases while the hole Hall areal density increases with laser ED, which indicates a higher degree of doping. Notably, regardless of the laser ED and number of pulses, a hole areal density between  $7 \times 10^{15} \text{ cm}^{-2}$  –  $13 \times 10^{15} \text{ cm}^{-2}$  was measured for B, whereas for Ga, the hole areal density is about one order of magnitude lower, ranging between  $0.9 \times 10^{15} \text{ cm}^{-2}$  –  $3 \times 10^{15} \text{ cm}^{-2}$ . Figure 6 reports the maximum active concentrations measured as above in different samples for Ga and B as a function of the corresponding maximum chemical concentrations (total atomic concentration). To calculate the maximum active doping concentration, a conversion factor called the Hall scattering factor,  $r_H$ , needs to be considered to obtain the true active carrier concentration, according to the relationship  $p = r_H p_H$  where  $p$  is the hole concentration, and  $p_H$  is the Hall hole concentration. The Hall scattering factor is an empirically determined quantity that depends on various scattering mechanisms and detailed band structure.<sup>[55,56]</sup>

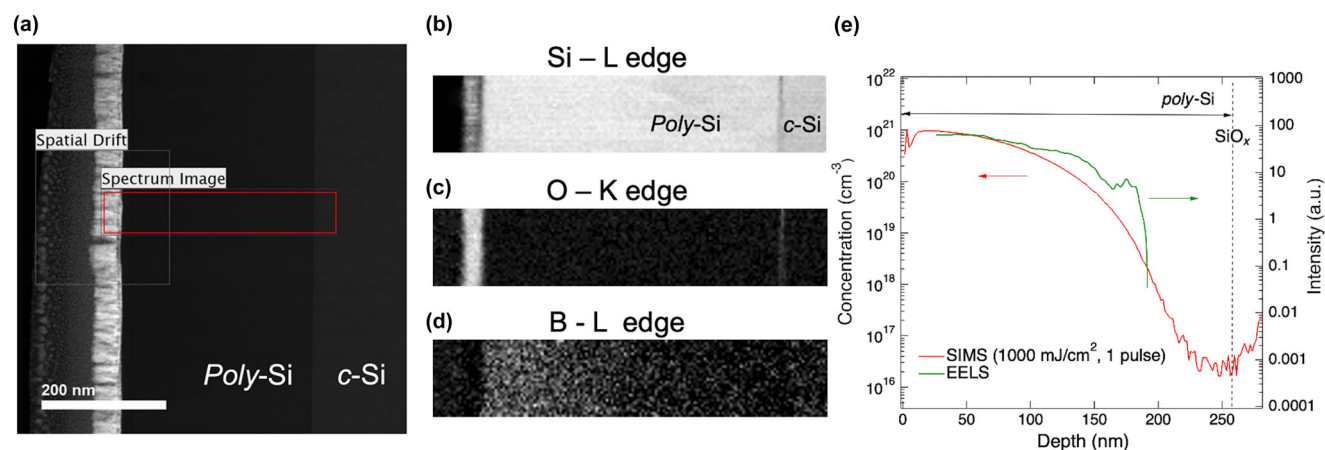


**Figure 4.** a) Cross-sectional HAADF image of the B laser processed sample. b) EELS mapping of Si – L edge. c) EELS mapping of O – K edge. d) EELS mapping of B – L edge. e) Comparison of doping concentration as a function of depth for SIMS and EELS line plot. The EELS mapping was averaged every 120 intervals.

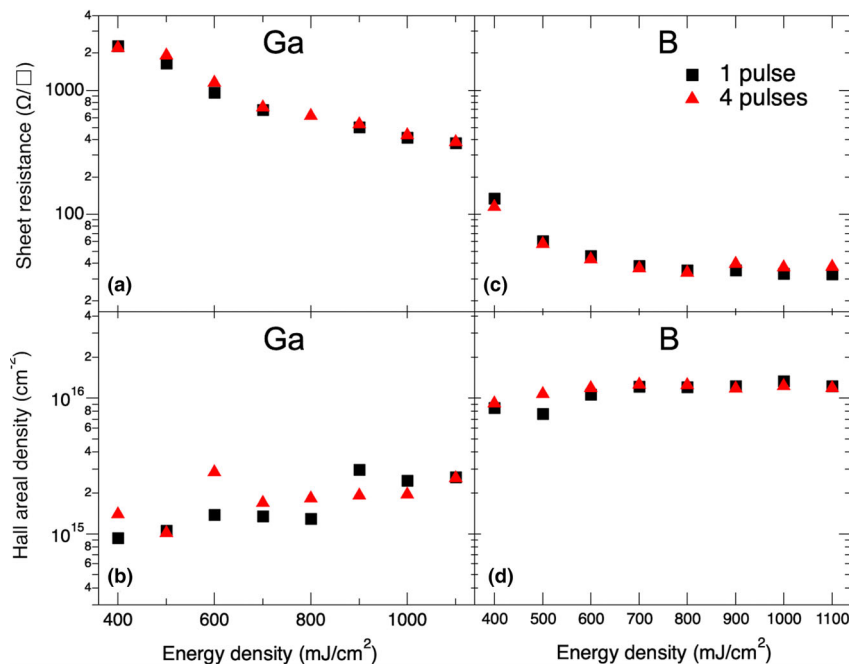


**Figure 5.** VdP-Hall measurements of Ga- a, b) and B- c, d) doped samples for different laser energy densities ranging from 400–1100  $\text{mJ cm}^{-2}$  and 1 or 4 pulses. a, c) Sheet resistance measurements. b, d) Hole areal density measurements.

Here, we assume a Hall scattering factor of  $r_H \approx 0.62$  based on a previous work by Romano et al., who determined  $r_H$  by fitting the Hall areal density and substitutional doping concentration for B and Ga in c-Si.<sup>[44]</sup> Taking  $r_H$  into consideration, we multiplied the hole Hall areal density in Figure 5 by  $r_H$  to obtain the true hole concentration for Ga and B. To compare the active dopant concentration to the total dopant concentration, we extract the maximum active dopant concentration,  $N_{\text{max}}$  (y-axis in Figure 6) using the SIMS profiles in Figure 3 following the procedure in Impellizzeri et al.<sup>[57]</sup> We assume that in regions with dopant concentration below  $N_{\text{max}}$ , 100% of the dopants are active (see inset in Figure 6). In the region closer to the surface, the dopant concentration in the SIMS profile is higher than  $N_{\text{max}}$ . We further assume that dopants at concentrations above  $N_{\text{max}}$  are inactive. We then integrate the SIMS profile with  $N_{\text{max}}$  set as the upper limit (see the shaded region in the inset of Figure 6) such that the integrated SIMS profile ( $\text{cm}^{-2}$ ) is equal to the measured active drift areal density obtained from the Hall measurements.<sup>[57]</sup> The maximum chemical concentrations in Figure 6 were calculated as the mean of the SIMS profiles in the top 10–25 nm after excluding the surface artifacts through extrapolation.

Boron at low chemical concentrations, up to  $\sim 5 \times 10^{20} \text{ cm}^{-3}$ , approaches nearly 100% activation, but the fraction of active dopants decreases to  $\sim 50\%$  at higher chemical concentration and levels off at  $\sim 10^{21} \text{ cm}^{-3}$ . This upper limit for B dopant activation is twice the solubility limit of B in Si. Conventional furnace annealed B-doped low pressure chemical vapor deposition (LPCVD) poly-Si in Hollemann et al.<sup>[58]</sup> reported  $\sim 75\%$  active B atoms, but at a lower doping concentration of  $\sim 5 \times 10^{19} \text{ cm}^{-3}$ . Our result is also much higher than the  $\sim 1.3\%$  activation level for B reported by Nemeth et al.<sup>[59]</sup> using conventional annealing in a furnace. In comparison, we show with PLM  $\sim 100\%$  of B atoms are activated in poly-Si at a much higher doping concentration of up to  $\sim 5 \times 10^{20} \text{ cm}^{-3}$ .

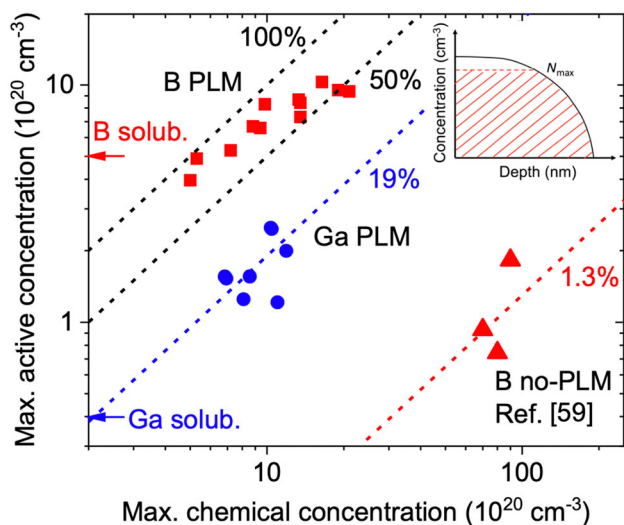
For Ga in Figure 6, there is no clear trend in the fraction of active Ga atoms in poly-Si. For a maximum chemical concentration confined in the relatively narrow range over  $7\text{--}12 \times 10^{20} \text{ cm}^{-3}$ , the corresponding active concentrations is over the range of  $1.2\text{--}2.5 \times 10^{20} \text{ cm}^{-3}$  (11%–24% activation). We ascribe this difference in dopant activation to lower solubility and low segregation coefficient ( $\sim 10^{-2}$ ) in solid Si/molten Si of Ga compared with B ( $\sim 1$ ). As the liquid–solid melt front moves towards the surface during recrystallization (see discussion for Figure 3a), Ga is pushed out from the growing solid into the remaining melt. This leads to the observed steeper Ga concentration depth profiles compared with the “box-like” depth profiles for B. This reduces the amount of Ga dopants in the poly-Si portion closer to the  $\text{SiO}_x$ /wafer interface. Nevertheless, 19% dopant activation level (averaged over the doped portion of poly-Si) in Figure 6 is almost six times higher than the Ga solubility limit (at 1200 °C). These values indicate that hyperdoping of Ga in poly-Si was successfully achieved via ion implantation and subsequent PLM with active dopant concentrations similar to those previously reported in c-Si.<sup>[49,50]</sup>

Figure 7 shows the hole drift mobilities as a function of the maximum hole concentration for

Ga and B, calculated from the data in Figure 5 using the expression  $\mu_D = 1/R_s e N_H r_H$ , where  $\mu_D$  is the hole drift mobility,  $R_s$  is the sheet resistance,  $N_H$  is the Hall areal density, and  $e$  is the electron charge. The Hall scattering factor,  $r_H$ , has been assumed equal to 0.62 according to Romano et al.<sup>[44]</sup> Figure 7 also shows hole drift mobility for Ga- and B-doped c-Si from previous studies.<sup>[60,61]</sup> These values differ from each other due to the lattice strain induced by the dopants, which in turn influences the hole effective mass. The same study<sup>[61]</sup> also extracted the strain-corrected mobility, i.e., the mobility for unstrained p-type doped Si, which is the same for both dopants. It is interesting to note that the B mobility data in poly-Si obtained in this work lie between the values reported in the literature for B in c-Si, and the trend depicted by the strain-corrected curve. We speculate that in the case of B the deviation from the c-Si curve towards the unstrained Si curve could be attributed to strain relaxation in poly-Si during the pulsed laser processing. On the contrary, the hole mobility for Ga-doped poly-Si is much lower than the trend in the c-Si and the strain-corrected curves. We attribute this to a lower activated fraction of Ga dopants and additional scattering channels that limit the carrier mobility, such as Ga clusters in the grain boundaries<sup>[62,63]</sup> and neutral impurity scattering.<sup>[64,65]</sup> Finally, comparing the B mobility data with Nemeth et al.,<sup>[59]</sup> which represents the state-of-the-art furnace-annealed PECVD poly-Si, the laser processed sample shows  $\sim$ four times higher mobility, again highlighting the advantage of using PLM.

### 2.3. Electron Microscopy of the Contact Structures

Figure 8 shows a backscattered electron image (Figure 8a) and an electron backscatter diffraction (EBSD) inverse pole figure (IPF) map (Figure 8b) for a Ga-sample using PLM at  $900 \text{ mJ cm}^{-2}$ . The image



**Figure 6.** Maximum hole concentration as a function of the maximum Ga and B chemical concentration obtained as described in the text. The blue, black and red dashed lines indicate the 19% activation trend for Ga, the full activation trend for B processed with PLM, and the 1.3% activated for B annealed with a conventional tube furnace. The continuous lines serve as a guide for the eye. The inset shows how the maximum active concentration was calculated. The blue and red arrows indicate the Ga and B solubility limit in Si, respectively.

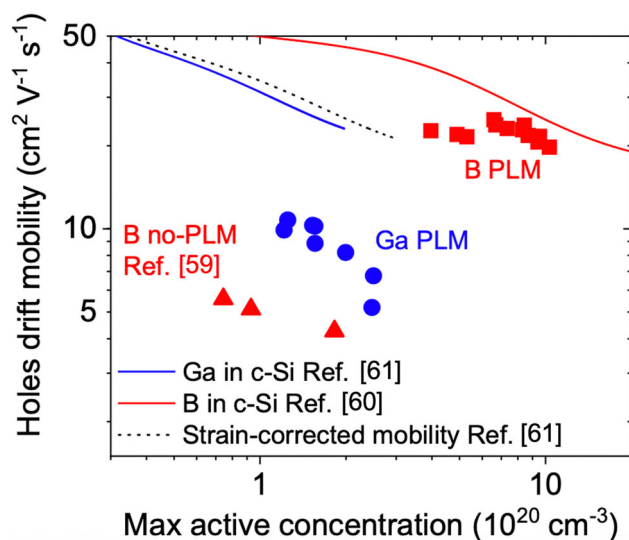


**Figure 7.** Hole drift mobility as a function of maximum active doping concentration for Ga (blue) and B (red). The solid red and blue lines indicate the trends in *c*-Si reported in Masetti *et al.*<sup>[60]</sup> and Romano *et al.*<sup>[61]</sup> for hole mobility of B and Ga in *c*-Si, respectively. The strain-corrected hole mobility in *c*-Si was also reported in Romano *et al.*<sup>[61]</sup> The blue circles and red squares indicate the Ga and B mobilities after PLM, respectively, and the red triangles indicate the B mobilities after conventional furnace annealing in Nemeth *et al.*<sup>[59]</sup>

contrast in Figure 8a arises from differences in orientation that cause the backscattered electrons to interact with varying degrees with the annular detector. In Figure 8b, the Kikuchi patterns generated by backscattered electrons are indexed relative to the silicon crystal

structure and each pixel is assigned a color related to the crystallographic direction that is normal to the sample surface. The black pixels represent regions where no solution was found based on the diffraction pattern at those pixels. This can occur when multiple small grains overlap within the volume where the diffraction pattern is generated. However, this does not seem to be the case for this sample. The diffraction pattern for the black regions does not contain any Kikuchi patterns (see Figure S1) which suggests that these regions could be amorphous. In general, EBSD shows that the laser annealed poly-Si has an average grain size of  $\sim 100$  nm.

To confirm that the sample structure (poly-Si/SiO<sub>x</sub>/*c*-Si) remained intact after laser processing, we performed cross-sectional transmission electron microscopy (TEM) on the Ga sample post laser processing, and the oxide interface was not impacted and stayed intact (see Figure S2).

We also performed PLM on randomly textured *c*-Si samples, which are otherwise nominally identical to the polished *c*-Si samples discussed above. The EDs used in these experiments were over the range of 200–500 mJ cm<sup>-2</sup>. Figure 9a shows the plan-view scanning electron microscopy (SEM) image of the laser-processed region. It is evident that the vertices of the pyramids are deformed. However, the simulated maximum melt depth at a higher ED of 700 mJ cm<sup>-2</sup> on a planar surface is <25 nm (see Figure 2a). Nevertheless, Figure 9b shows that  $\sim 500$ –600 nm of the *c*-Si pyramid melted and recrystallized. The melting behavior at the vertices of the pyramids indicates that the pyramid tips have been subjected to a temperature above the melting point of Si. We attribute this difference to the heat dissipation at the pyramid tips versus the faces or valleys. For a given ED, the heat flux to a textured surface is lower because of a higher surface area by a factor of  $\sim \sqrt{3}$  compared with a planar surface. However, at the pyramid tips, there are four melt fronts corresponding to each pyramid face that converge, and with no heat dissipation into the bulk *c*-Si, this causes melting over a much larger length scale than a planar surface. Once the tips melt, the liquid surface tension tends to round off the surface and modifies the shape of the vertices. This deformation of the pyramid tips also resulted in poor passivation, which was confirmed by photoluminescence imaging (Figure S3). SIMS and VdP-Hall measurements show that the lower ED (200–500 mJ cm<sup>-2</sup>) used in PLM of textured samples was not as effective in spreading and activating the Ga dopants (see Figures 3a and 5b). Therefore, we conclude that textured samples require careful tuning of the laser conditions to preserve passivation, and this technique is more suitable for the planarized back surface.

#### 2.4. Passivation Quality of Ga-Doped Contacts

Figure 10a shows the photoluminescence (PL) image of a Ga-doped polished sample after PLM and a 2nd passivation for different ED and number of pulses. Most of the laser-processed  $5.1 \times 5.1$  mm<sup>2</sup> regions (see Figure 1b) appear bright in this image except for those that are close to the edges. To qualitatively analyze the passivation quality of each region, we first determine the change in the  $iV_{oc}$ ,  $\Delta iV_{oc}$ , by using the PL intensity of each laser processed spot before PLM ( $I_{PL\ before}$ ) and after PLM ( $I_{PL\ after}$ ) in the expression in Equation 1.<sup>[66]</sup>

$$\Delta iV_{oc} = \frac{kT}{q} \ln \left( \frac{I_{PL\ after}}{I_{PL\ before}} \right) \quad (1)$$

In this expression,  $k$  is the Boltzmann's constant,  $T$  is the temperature of the sample,  $q$  is the unit charge of an electron. Using

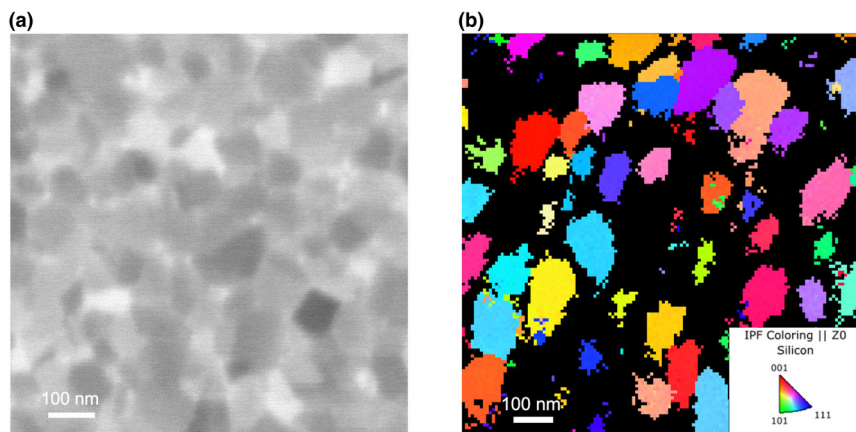


**Figure 8.** a) Plan-view SEM image b) EBSD inverse pole figure map of the Ga-laser processed sample. The different colors represent different *c*-Si orientations with the IPF coloring scale at the lower bottom right. Black regions were not able to be indexed.

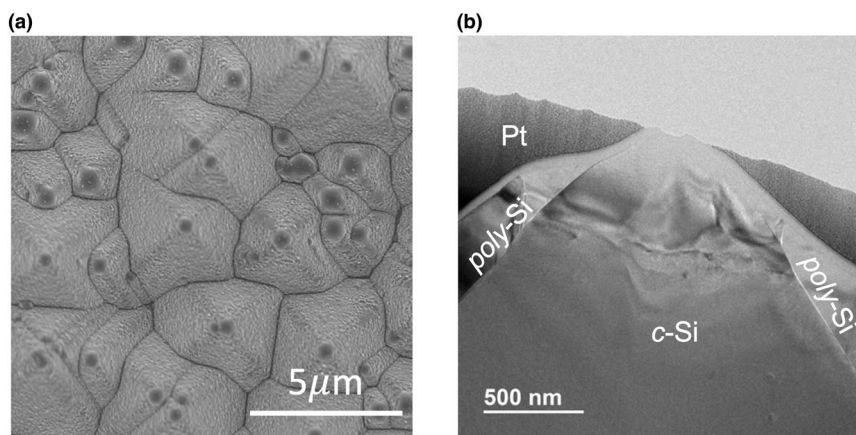


**Figure 9.** a) SEM image on textured sample with low energy density of 200–500 mJ/cm<sup>2</sup>. b) Cross-sectional TEM image of the pyramidal structure after laser processing. The estimated location of *poly*-Si, *c*-Si, and Pt are labeled. Note only the ED range was given due to the inability of distinguishing various laser spots under SEM.

photoconductance decay measurement, we determined the  $iV_{oc}$  of a larger sample that was processed in a similar manner as the one in Figure 10a, except that it did not undergo PLM. For each laser processed spot in Figure 10a, the absolute  $iV_{oc}$  is obtained by adding  $\Delta iV_{oc}$  to the reference sample's  $iV_{oc}$ . We see that the PL brightness increases with increasing laser ED but adding additional laser pulses had little effect on the passivation. The field regions around the laser processed spots appear darker indicating that the passivation quality of the laser annealed regions is better than the surrounding field regions. The highest  $iV_{oc}$  value of 721 mV was achieved with a pre-PLM passivation anneal, for a laser ED of 900 mJ cm<sup>-2</sup> and 4 pulses. The  $iV_{oc}$  values listed here are an average of the passivation quality of both the rough and PLM-processed sides of the wafer. The passivation quality of the back rough side of these single-side-polished samples was not measured, and likely lowered the measured  $iV_{oc}$ . Therefore, the  $iV_{oc}$  values listed in Figure 10a are conservative and the actual passivation of the PLM surface is likely much higher. The tube furnace processed witness

samples have an  $iV_{oc}$  of 716 and 700 mV for Ga- and B-doped samples, respectively.

To extend PLM processing to a larger area, we used overlapping laser square spots across the *c*-Si wafer. We used an ED of 900 mJ cm<sup>-2</sup> and 2 pulses at each position, which resulted in four PLM pulses at the edges, and eight PLM pulses at the corners of the squares. Figure 10b shows the PL image of a 30 × 50 mm<sup>2</sup> sample after PLM rastering. A part of this sample was not laser processed for comparison. The  $iV_{oc}$  of the laser-processed region of the sample was 735 mV, with a  $J_0$  value of 4.1 fA/cm<sup>2</sup>, which is even higher than the  $iV_{oc}$  for the small laser processed spot shown in Figure 10a. Remarkably, the PL intensity is uniform across the sample without any deterioration in passivation of the edges or corners of the individual laser spots due to the overlapping laser positions. The PL intensity for the non-laser processed region is darker than the laser processed region, which is expected due to the lack of dopant activation. This result demonstrates our ability to PLM large area samples and lays the groundwork for incorporating it into a back-junction front/back *poly*-Si/SiO<sub>x</sub> passivating contacts device – such as high-performance *p*-type TOPCon solar cells.

## 2.5. Electrical Characterization of Ga-Doped Contacts

The metal-to-*poly*-Si contact resistivity for *poly*-Si:Ga/SiO<sub>x</sub> contacts on *n*-type wafers was determined to be 0.9 mΩ•cm<sup>2</sup> using the transfer length method (TLM)<sup>[67]</sup> on the sample shown in Figure 10b. To extract the *poly*-Si-to-*c*-Si contact resistivity, we evaporated 1 μm thick dots of Ti/Ag of varying sizes (35 μm, 70 μm, 0.125 mm, 0.5 mm, and 1 mm; see inset of Figure 11a) onto each laser processed spot for the sample shown in Figure 10a. Isolated diode structures were produced by etching the unmetallized *poly*-Si:Ga/SiO<sub>x</sub> contacts into the *c*-Si wafer using an SF<sub>6</sub> plasma (see inset of Figure 11b). An ohmic contact was also formed on the back of the sample by etching off the *poly*-Si/SiO<sub>x</sub> and contacting the bulk *c*-Si with a Ga-In eutectic alloy. Current-voltage (*I*-*V*) measurements were performed for the diode structures by contacting the circular electrode at the front and the Ga-In eutectic at the back. The contact resistivity was obtained from Equation (2)<sup>[68]</sup> by plotting  $dV/d\ln(I)$  versus *I* for various sized metal contacts (see Figure 11a).

$$\frac{dV}{d\ln(I)} = R_T I + \frac{nq}{kT} \quad (2)$$

In Equation 2,  $R_T$  is the total resistance, which can be obtained from the slope of each curve, and  $n$  is the ideality factor.<sup>[68]</sup>  $R_T$  is a combination of diode resistance  $R_{diode}$ , spreading resistance  $R_s$ , and the resistance

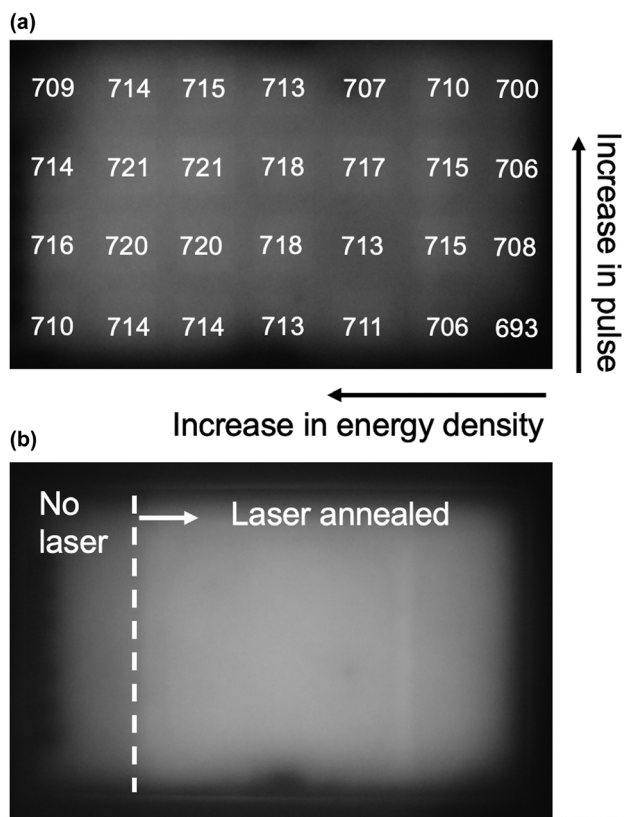


**Figure 10.** a) PL image of a polished Ga-doped *poly-Si/SiO<sub>x</sub>* test structure shown in Figure 1b. The numbers indicate the  $iV_{oc}$  values in mV for each laser processed spot. b) PL image of a large-area, laser-processed sample using two laser pulses at an energy density of  $900 \text{ mJ cm}^{-2}$ . The area to the left of the dashed white line was not laser processed for comparison. Exposure time: 1/10 s. Note both samples received a 2nd passivation with  $\text{Al}_2\text{O}_3$  and FGA.

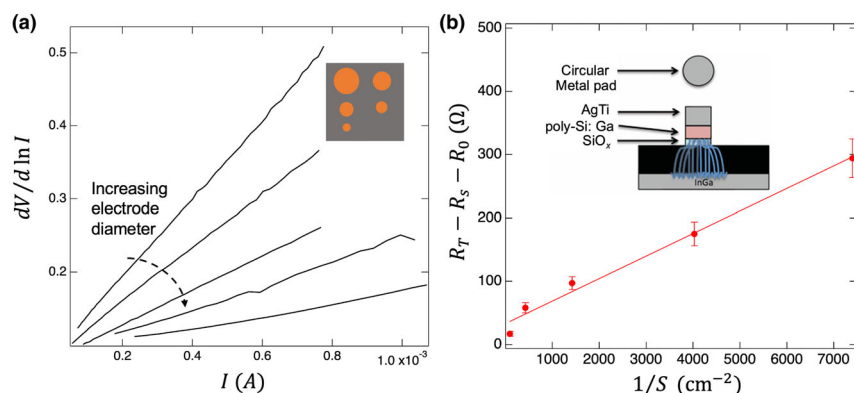


**Figure 11.** a) A plot of  $dV/d\ln(I)$  vs  $I$  for circular electrodes of increasing diameter. The measurements were made on a single  $5.1 \times 5.1 \text{ mm}^2$  spot that was laser processed with four pulses at an energy density of  $900 \text{ mJ cm}^{-2}$  (spot 5, C in Figure 1b). The inset shows five metal contacts with varying diameters deposited on a single laser processed spot. b) A plot of  $R_T - R_S - R_0$  versus  $1/S$  ( $S$ -area of circular electrode) with a linear fit. The slope of the fitted line provides the contact resistivity. The inset shows the schematic of the cross-section of the test structure after isolation of each circular electrode by etching the *poly-Si*,  $\text{SiO}_x$  and the top few nanometers of the *c-Si* wafer with a  $\text{SF}_6$  plasma.

of the wafer and the bottom contact  $R_0$ .  $R_s$  was determined according to Denhoff<sup>[69]</sup> and  $R_0$  was measured by bypassing the diode region of the sample and directly contacting the bulk *c-Si*. The five different values of  $R_{\text{diode}} = R_T - R_S - R_0$  are plotted as a function of  $1/S$ , where  $S$  is the area of the circular electrodes (see Figure 11b) to obtain the average contact resistivity. For an ED of  $900 \text{ mJ cm}^{-2}$  and 4 pulses (laser spot “5, C” in Figure 1b), the contact resistivity is  $35.5 \pm 2.4 \text{ m}\Omega \text{ cm}^{-2}$ . B-doped samples were analyzed similarly, resulting in a lower contact resistivity of  $13.6 \pm 5.2 \text{ m}\Omega \text{ cm}^{-2}$ . We only report the best contact resistivity values due to the inability to measure this quantity on laser spots with lower dopant activation. The low contact resistivity is consistent with the Hall data for B (see Figure 5c,d) where the sheet resistance is low with a high hole areal density. Interestingly, both B and Ga SIMS profiles in Figure 3 show a lowly doped *poly-Si* region (below the SIMS background of  $10^{17} \text{ cm}^{-3}$ ) near the tunneling  $\text{SiO}_x$ . Yet, despite this lowly doped *poly-Si* region, we obtained low contact resistivity for both Ga and B.

To validate the resistivity measurements for the Ga sample that was laser processed with an ED of  $900 \text{ mJ cm}^{-2}$  and 4 pulses, we performed cross-sectional scanning spreading resistance microscopy (SSRM) to probe the local spreading resistance as a function of depth from the metal electrode into the Ga-doped *poly-Si* film (schematic in Figure 12a). Due to the small atomic force microscopy (AFM) tip-sample contact area, the resistance measured by SSRM is dominated by the resistivity of local sample volume right beneath the probe in nm-scale. Figure 12b shows a spreading resistance map over a  $1 \times 1 \mu\text{m}^2$  region. In this image, the metal appears dark (low resistance) and the *c-Si* wafer, which has a much higher resistivity, appears lighter (high resistance). This sharp change in resistance occurs within the *poly-Si*. In the 1D line scan shown in Figure 12c, we can see that within the Ga-doped *poly-Si* contact, there is a high resistance region with a low doping concentration that is closer to the *c-Si* wafer that spans from about 100–150 nm. Thus, SSRM results confirm that the resistance profile is consistent with the SIMS depth profiles in Figure 3a.

Typically, low contact resistivity is achieved in *poly-Si/SiO<sub>x</sub>* contacts when the *poly-Si* is heavily doped, and dopants diffuse through the  $\text{SiO}_x$  and form a sharp decreasing gradient tail inside the *c-Si*. However, our

results show that despite a lowly doped *poly-Si* region in-between the heavily doped *poly-Si* and the  $\text{SiO}_x$ , a relatively low contact resistivity of  $<40 \text{ m}\Omega \cdot \text{cm}^2$  is obtained. To better understand the transport in these PLM-processed samples, we performed Kelvin probe force microscopy (KPFM) measurements on the structure shown in the inset of Figure 13a to map the electric field across the p-n junction. The height profile across the cross-section of the sample is shown in Figure 13a, which can be used to distinguish between the metal and *poly-Si* region due to the surface morphology difference of metal and Si on the cross-section of the device. Figure 13b represents the electric field, which is the first derivative of the measured potential. The maximum of the electric field curves indicates the transition of the p-type to n-type semiconductor, and the overall shape of the electric field curves is directly correlated to the carrier concentration profiles around the p-n junction. Three different reverse bias voltages were applied to measure the electric field changes induced by the bias



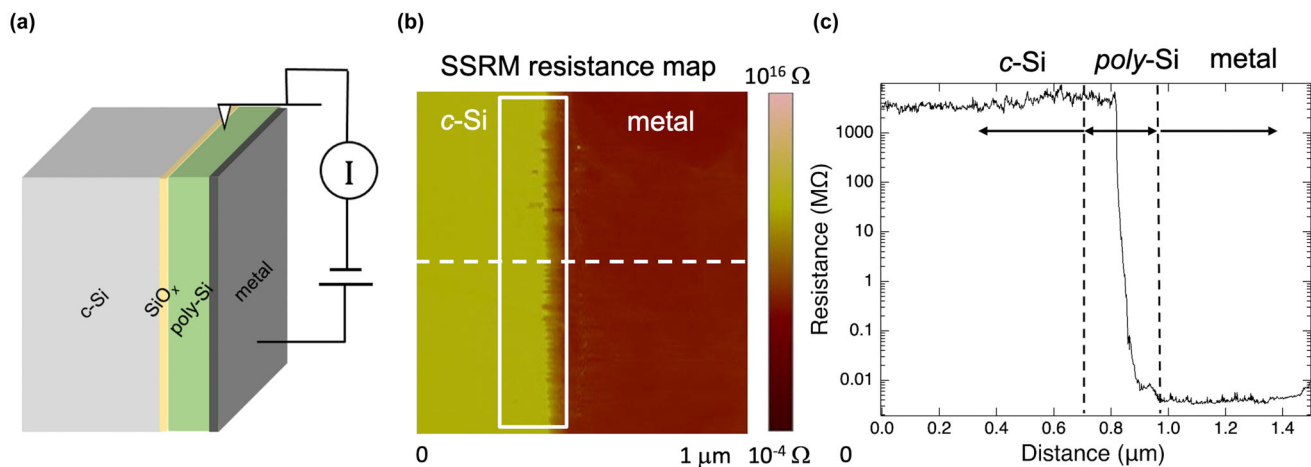


**Figure 12.** a) Schematic of the setup for scanning spreading resistance microscopy (SSRM). b) SSRM resistance map with the magnitude of resistance indicated by the color scale bar on the right. The region inside the white box indicates the location of *poly-Si*. c) Line plot of the SSRM measurement showing the resistance values in  $M\Omega$  as a function of the distance from the top electrode. The dashed black lines and arrows indicate the locations for metal, *poly-Si*, and *c-Si*.

voltages in order to minimize the effect of surface charges trapped on the cross-sectional surface. All three curves show a peak at  $\sim 450$  nm, which is  $\sim 250$  nm from the metal/*poly-Si* interface. Given that the *poly-*

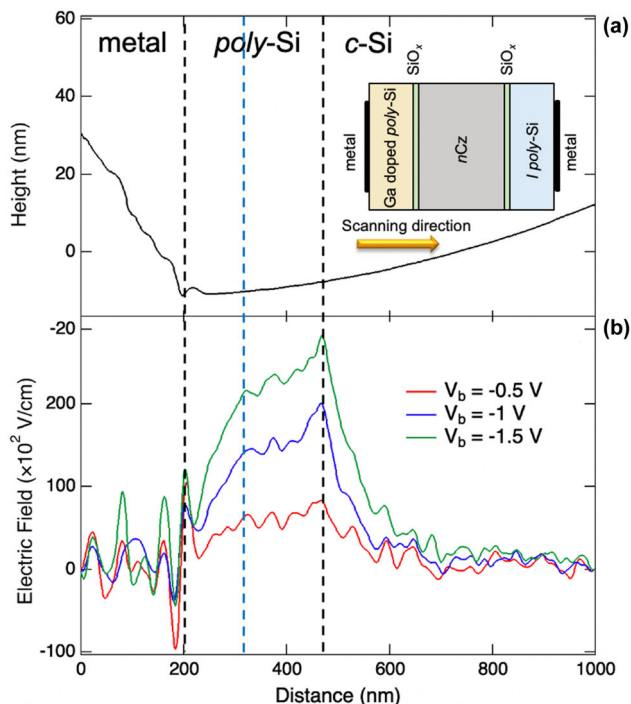


**Figure 13.** a) Atomic force microscopy data showing height as a function of distance from the top metal electrode. The inset indicates the cross-sectional device structure for KPFM measurement. b) Electric field results as a function of distance for three reverse bias voltages. The red (—), blue (—), and green (—) solid lines indicate reverse bias voltage of  $-0.5$  V,  $-1$  V, and  $-1.5$  V respectively. The dashed black lines indicate the locations of metal, *poly-Si*, and *c-Si*. The laser condition for the sample used for KPFM measurement is  $900 \text{ mJ cm}^{-2}$  and 1 pulse (thick purple dashed line in Figure 3a).

Si has a thickness of  $\sim 250$  nm, the transition from *p-* to *n-*type Si occurs around the interface between *poly-Si*/ $\text{SiO}_x$  contact and the *n-*type *c-Si* wafer. Interestingly, for all three bias voltages, the electric field decays much more slowly into the *poly-Si* region than into the *c-Si* region, which suggests that most of the depletion region lies within *poly-Si*, with a small portion extending into *c-Si*. The slope of the electric field also decays slower from the *poly-Si*/*c-Si* interface to the blue line, which indicates that the *poly-Si* closer to the oxide is lowly doped. The slopes of the field increase after the blue line to the interface between metal and *poly-Si*, which shows that the *poly-Si* near the metal surface is more heavily doped. These results are again in agreement with the SSRM data in Figure 13c and the SIMS profiles in Figure 3a.

In our electrical measurement, we are detecting the diffusion-limited recombination current into the  $p^+$  *poly-Si*/ $\text{SiO}_x$  contact, similar to the classical diode dark current. However, in this measurement we cannot establish relative contributions to the overall current from electrons and holes. At this point, we can conclude that the hyperdoped contact passes the recombination current at low apparent contact resistivity. Hole transport properties can be established separately in a solar cell device or on *p-*type wafer, which is planned for future work.

### 3. Conclusion

In this work, we demonstrated a novel *poly-Si*:Ga/ $\text{SiO}_x$  passivating contact through non-equilibrium doping enabled by PLM. We explored a range of laser energy densities from  $300$  to  $1100 \text{ mJ cm}^{-2}$  and laser pulses (1–6) to optimize the melt depth and the resulting Ga and B depth profiles in *poly-Si*. The SIMS depth profiles indicate that higher ED and number of pulses promote dopant penetration into the depth of *poly-Si* and allow hyperdoping within the *poly-Si*. VdP-Hall measurements reveal active doping concentrations as high as  $\sim 2.5 \times 10^{20} \text{ cm}^{-3}$  for Ga and  $\sim 10^{21} \text{ cm}^{-3}$  for B. The active dopant fraction for B in *poly-Si* approached  $\sim 100\%$  up to a chemical concentration of  $5 \times 10^{20} \text{ cm}^{-3}$  after which the activated fraction decreased to  $\sim 50\%$  for a chemical concentration of  $\sim 2 \times 10^{21} \text{ cm}^{-3}$ . This high fraction of activated B dopants in *poly-Si* beyond the solubility limit combined with

*c*-Si-like hole mobilities has been reported for the first time. For Ga, we report hyperdoping 6× above the solubility limit but with active dopant fractions between 11%–24%, and lower mobilities likely due to Ga clusters in the grain boundaries and neutral impurity scattering. These results unambiguously demonstrate that PLM can be used for hyperdoping of poly-Si with Ga and B. Despite the melt/freeze cycle of the poly-Si during PLM processing, the passivation of the SiO<sub>x</sub>/*c*-Si interface remained high or improved with annealing. For the Ga-doped poly-Si/SiO<sub>x</sub> contacts on polished *n*-type Cz *c*-Si wafers, we demonstrated a high *i*V<sub>oc</sub> of 735 mV. Electron microscopy and photoluminescence measurements show that alkaline-textured Si(100) surfaces with random pyramids require additional work with PLM due to melting and deformation of the pyramid tips as the ~500 nm melt region penetrates well beyond the SiO<sub>x</sub> layer and degrades the chemical passivation. Additionally, we extended PLM to a larger 3 × 4 cm<sup>2</sup> area by patching together multiple 5.1 × 5.1 mm<sup>2</sup> spots and showed good passivation quality with no degradation from the overlapping laser spots at the edges and corners. For Ga-doped poly-Si/SiO<sub>x</sub> contacts, there was a lowly doped poly-Si region of ~100 nm between the hyperdoped surface region and the SiO<sub>x</sub>/*c*-Si interface. Nevertheless, we obtained a contact resistivity of 35.5 ± 2.4 mΩcm<sup>2</sup>, using the expanded Cox and Strack method. We also tested the metal-to-semiconductor contact resistivity using TLM and obtained a low value of 0.9 mΩ cm<sup>-2</sup>. We think that the hyperdoped contact passes the recombination current at low apparent contact resistivity, but further investigation is needed. Overall, this result shows that by using PLM a sufficiently low contact resistivity can be obtained for Ga-doped poly-Si contacts compared with the ~10 Ω cm<sup>2</sup> resistivity obtained by conventional furnace annealing.<sup>[32]</sup> Therefore, PLM is a promising technique for the fabrication of Ga-doped poly-Si/SiO<sub>x</sub> passivating contacts that can address the lower *i*V<sub>oc</sub> obtained for conventionally annealed B-doped poly-Si/SiO<sub>x</sub> passivating contacts.

#### 4. Experimental Section/Methods

**Fabrication of test structures:** Both double-side textured (180 μm) and single-side polished (400 μm) phosphorus-doped, 3–5 Ω·cm resistivity, Czochralski (Cz) Si wafers (Woongjin) were cleaned with piranha and the standard RCA method.<sup>[70,71]</sup> A ~1.5 nm low-temperature SiO<sub>x</sub> layer was then formed on both sides of the wafer, followed by the growth of ~200 nm of intrinsic poly-Si on textured samples and ~250 nm of intrinsic poly-Si on polished samples via low-pressure chemical vapor deposition. Subsequently, both textured and polished Si wafers were laser-scribed into 30 × 50 mm pieces. These wafers were then split into two groups. For the first group, we deposited ~20 nm of B-doped hydrogenated amorphous Si (*a*-Si:H) on one side via PECVD using a SiH<sub>4</sub>/H<sub>2</sub>/B<sub>2</sub>H<sub>6</sub> capacitively-coupled, radio-frequency (rf) plasma operating at 13.56 MHz and a pressure of 1 Torr. The *c*-Si wafers were placed on the grounded electrode, which was kept at 300 °C. The plasma power was 8 W, and the gas flow rates were set to 2 and 100 standard cm<sup>3</sup>/min (sccm) for SiH<sub>4</sub> and H<sub>2</sub>, respectively, with 1 sccm of B<sub>2</sub>H<sub>6</sub> (2.6% in H<sub>2</sub>). For the second group of samples, <sup>69</sup>Ga ions were implanted at 10 keV with a nominal dose of 6 × 10<sup>15</sup> cm<sup>-2</sup>. However, the implanted Ga dose measured by Rutherford backscattering spectrometry (RBS) was found to be 4.5 ± 0.2 × 10<sup>15</sup> cm<sup>-2</sup> (see Figure S4) which is ~25% lower than the nominal implant dose. We attributed this loss of Ga to the sputtering of the highly doped poly-Si surface layer during ion implantation. To limit the projected depth to <50 nm, the implant energy and doses were estimated using simulations with the Stopping Range of Ions in Matter (SRIM-2013) software.<sup>[72]</sup>

Both Ga-doped and B-doped samples were further split into two groups: one group was used for PLM studies and the second group was annealed in a tube furnace. Prior to pulsed laser melting, ~15 nm of Al<sub>2</sub>O<sub>3</sub> was deposited on the Ga-implanted samples using atomic layer deposition (ALD) from

trimethylaluminum and water. This was followed by annealing in forming gas (1:9 H<sub>2</sub>:N<sub>2</sub>) at 400 °C for 60 min. After annealing, the Al<sub>2</sub>O<sub>3</sub> was removed in a 1% aqueous HF solution. Both Ga- and B-doped samples underwent PLM with a KrF excimer laser (λ = 248 nm) and a pulse duration of 22 ns (based on full width at half maximum). The laser has a spot size of 5.1 × 5.1 mm<sup>2</sup> with a uniformity within 2%. Figure 1a shows a schematic of Ga- and B-doped test structures that were processed with the excimer laser. The samples were translated laterally using a motorized X-Y stage to process multiple locations with varying energy densities and numbers of pulses. The matrix of the varying laser conditions on a 30 × 50 mm<sup>2</sup> test sample is illustrated in Figure 1b, which features seven columns with different laser EDs and four rows corresponding to different numbers of laser pulses. After laser processing, the final test structure is shown in Figure 1c. For comparison purposes, the second set of ion-implanted samples was annealed in a tube furnace at 850 °C for 30 min in N<sub>2</sub> ambient to crystallize the *a*-Si:H into poly-Si, and to diffuse and activate dopants. The samples were re-passivated by Al<sub>2</sub>O<sub>3</sub> deposited by ALD and annealed in forming gas.

**Simulation of laser processed temperature-depth profiles:** Simulations based on heat flow calculations were performed by inputting physical and optical data for Si from literature into the LIMP-Laser Induced Melting Prediction, the Harvard simulation software package.<sup>[73]</sup> We assume that the ~200 nm layer of poly-Si has properties similar to *c*-Si. In this model, there is a 20 nm *a*-Si:H layer on top of poly-Si. We assume a flat surface with a reflectivity *R* = 0.67. The maximum melt depth profiles were modeled with laser EDs between 700–1100 mJ/cm<sup>2</sup>.

**Characterization of the test structures:** The Ga and B depth profiles in the test structures were analyzed using SIMS with a 3 keV O<sub>2</sub><sup>+</sup> beam, collecting <sup>69</sup>Ga<sup>+</sup>, <sup>11</sup>B<sup>+</sup>, <sup>16</sup>O<sup>+</sup>, and <sup>30</sup>Si<sup>+</sup> secondary ions. The Ga concentration was calibrated by measuring the as-implanted Ga dose in selected samples by RBS, and the calibration of the B concentration was performed by measuring a certified standard. For both elements, the concentrations have a relative error of ±10%. The depth scales were calibrated with an accuracy of ±1% by measuring the crater depths with a profilometer (Tencor P17) and assuming a constant sputtering rate. The sheet resistance, carrier areal density and mobility of the dopants were determined by VdP-Hall measurements, using a 0.65 T permanent magnet, with relative errors of ±5%. The Ga doped samples were further analyzed using the following techniques. PL was used to map the passivation quality for different laser processing conditions.<sup>[74]</sup> The PL intensity for different laser processed spots was used to calculate the *i*V<sub>oc</sub> by comparing it to a larger control sample that was annealed in the tube furnace.<sup>[66]</sup> The *i*V<sub>oc</sub> for this control sample was determined using quasi-steady state photoconductance (QSSPC) decay measurements performed using a Sinton WCT-120 instrument at 1-Sun illumination.<sup>[75–78]</sup> The contact resistivity was determined using the expanded Cox and Strack method described by Wang *et al.*<sup>[68]</sup> Cross-section SEM was performed using Hitachi S-4800 FE-SEM. TEM specimens were prepared by the focused ion beam (FIB) lift-out technique using a Nova 200 Nanolab Dual-Beam FIB.<sup>[79]</sup> Bright-field and phase-contrast TEM images were acquired using a FEI Tecnai F20 TEM operated at 200 kV. EELS spectrum imaging was performed using a Gatan Enfium spectrometer with dispersion set to 0.25 eV/channel an acquisition time of 0.2 s at each pixel and an approximate pixel size of 2 nm within the map regions. EBSD mapping was performed on a FEI Nova 200 Nanolab dual-beam focused ion beam (FIB) equipped with an Oxford Nordlys detector. Data were collected using an accelerating voltage of 15 kV and beam current of 2.2 nA. EBSD data were processed using Oxford's AZtecICE software package.

The poly-Si region was characterized by cross-section SSRM<sup>[80]</sup> (Veeco Instruments Dimension 5000 scanning probe microscope with a Bruker SSRM module) to determine the local resistivity across the metal, poly-Si, and *c*-Si. The microscope was housed in an Ar glovebox (<0.1 ppm O<sub>2</sub>, <0.1 ppm H<sub>2</sub>O) to prevent oxidation of the sample. A conductive wear-resistant diamond-coated probe (Bruker DDESP-V2 nanoelectrical) with a radius of ~25 nm, was used for the SSRM measurements. The actual probe/sample contact size is usually smaller than the probe radius, giving better spatial resolution than the probe radius. The SSRM measurement was performed at an applied direct current bias of 3 V. All scans were conducted incrementally in 1 × 1 μm<sup>2</sup> scan areas. Additionally, cross-sectional KPFM was employed for potential imaging of the metallized test structure. The KPFM setup includes the first resonant oscillation of the Ptlr-coated cantilever (50–70 kHz), which was used for noncontact atomic force microscopy (AFM, Veeco D5000 and Nanoscope V) topographic imaging, and the second resonant frequency (300–500 kHz) for potential imaging, which yields an enhanced

energy resolution of ~10 mV. Three reverse bias voltages of -0.5, -1, and -1.5 V were applied to the device to measure the change in the potential as a function of distance from the metal surface.

## Acknowledgements

K.C. and E.N. contributed equally to this work. The author would like to thank Matthew B. Hartenstein from Colorado School of Mines for the processing of TLM masks, and L. Bacci and N. Argiolas from the University of Padova for technical support. This work was authored in part by the National Renewable Energy Laboratory, operated by Alliance for Sustainable Energy, LLC, for the U.S. Department of Energy (DOE) under Contract No. DE-AC36-08GO28308. Funding provided by the U.S. Department of Energy Office of Energy Efficiency and Renewable Energy Solar Energy Technologies Office. The views expressed in the article do not necessarily represent the views of the DOE or the U.S. Government. The U.S. Government retains and the publisher, by accepting the article for publication, acknowledges that the U.S. Government retains a nonexclusive, paid-up, irrevocable, worldwide license to publish or reproduce the published form of this work, or allow others to do so, for U.S. Government purposes. This work has been partially funded by the University of Padova through the grant UNIPD-ISR 2017 'SENSITIZE'.

## Conflict of Interest

The authors declare no conflict of interests.

## Supporting Information

Supporting Information is available from the Wiley Online Library or from the author.

## Keywords

Ga hyperdoping, Ga passivating contacts, poly-Si/SiO<sub>x</sub>, pulsed laser melting, silicon solar cell

Received: May 22, 2022

Revised: August 19, 2022

Published online: September 11, 2022

- [1] T. G. Allen, J. Bullock, X. Yang, A. Javey, S. De Wolf, *Nat. Energy* **2019**, 4, 914.
- [2] M. Hermle, F. Feldmann, M. Bivour, J. C. Goldschmidt, S. W. Glunz, *Appl. Phys. Rev.* **2020**, 7, 21305.
- [3] C. Battaglia, A. Cuevas, S. De Wolf, *Energ. Environ. Sci.* **2016**, 9, 1552.
- [4] A. W. Blakers, A. Wang, A. M. Milne, J. Zhao, M. A. Green, *Appl. Phys. Lett.* **1989**, 55, 1363.
- [5] P. Stradins, S. Essig, W. Nemeth, B. G. Lee, D. Young, A. Norman, Y. Liu, J.-W. Luo, E. Warren, A. Dameron, V. LaSalvia, M. Page, A. Rohatgi, A. Upadhyaya, B. Rounsaville, Y.-W. Ok, S. Glunz, J. Benick, F. Feldmann, M. Hermle, Passivated tunneling contacts to N-type wafer silicon and their implementation into high performance solar cells: preprint, **2014**.
- [6] U. Römer, R. Peibst, T. Ohrdes, B. Lim, J. Krügener, E. Bugiel, T. Wietler, R. Brendel, *Sol. Energy Mater. Sol. Cells* **2014**, 131, 85.
- [7] J. Schmidt, R. Peibst, R. Brendel, *Sol. Energy Mater. Sol. Cells* **2018**, 187, 39.
- [8] A. Richter, R. Müller, J. Benick, F. Feldmann, B. Steinhauser, C. Reichel, A. Fell, M. Bivour, M. Hermle, S. W. Glunz, *Nature Energy* **2021**, 6, 429.
- [9] R. Peibst, U. Römer, Y. Larionova, M. Rienäcker, A. Merkle, N. Folchert, S. Reiter, M. Turcu, B. Min, J. Krügener, D. Tetzlaff, E. Bugiel, T. Wietler, R. Brendel, *Sol. Energy Mater. Sol. Cells* **2016**, 158, 60.
- [10] F. Feldmann, M. Bivour, C. Reichel, M. Hermle, S. W. Glunz, *Sol. Energy Mater. Sol. Cells* **2014**, 120, 270.
- [11] A. Richter, J. Benick, R. Müller, F. Feldmann, C. Reichel, M. Hermle, S. W. Glunz, *Prog. Photovolt. Res. Appl.* **2018**, 26, 579.
- [12] Y. Chen, D. Chen, C. Liu, Z. Wang, Y. Zou, Y. He, Y. Wang, L. Yuan, J. Gong, W. Lin, X. Zhang, Y. Yang, H. Shen, Z. Feng, P. P. Altermatt, P. J. Verlinden, *Prog. Photovolt. Res. Appl.* **2019**, 27, 827.
- [13] Y. Chen, D. Chen, P. Altermatt, G. Xu, Z. Wang, C. Liu, Y. Zou, Y. He, Y. Wang, J. Gong, L. Yuan, W. Liu, Y. Chen, M. Deng, Y. Hu, S. Chen, J. Xiang, H. Shen, S. Zhang, L. Wang, X. Zhang, Y. Yang, Z. Feng, P. Verlinden, >25% large-area industrial silicon solar cell: learning from history and future perspective. in 36th EU PVSEC at: Marseille, France, **2019**.
- [14] D. Chen, Y. Chen, Z. Wang, J. Gong, C. Liu, Y. Zou, Y. He, Y. Wang, L. Yuan, W. Lin, R. Xia, L. Yin, X. Zhang, G. Xu, Y. Yang, H. Shen, Z. Feng, P. P. Altermatt, P. J. Verlinden, *Sol. Energy Mater. Sol. Cells* **2020**, 206, 110258.
- [15] L. E. Bellini, JinkoSolar achieves 26.1% efficiency for n-type TOPCon solar cell. in PV magazine, ed. online, **2022**. Available: <https://www.pv-magazine.com/2022/10/13/jinkosolar-achieves-26-1-efficiency-for-n-type-topcon-solar-cell/>.
- [16] A. Richter, J. Benick, F. Feldmann, A. Fell, and B. Steinhauser, Both sides contacted silicon solar cells: options for approaching 26% efficiency. in 36th European PV Solar Energy Conference and Exhibition, Marseille, France, **2019**.
- [17] Y.-Y. Huang, Y. W. Ok, K. Madani, W. Choi, A. Upadhyaya, V. Upadhyaya, B. Rounsaville, V. Chandrasekaran, A. Rohatgi, *Sol. Energy Mater. Sol. Cells* **2021**, 230, 111183.
- [18] Z. P. Ling, Z. Xin, P. Wang, R. Sridharan, C. Ke, and R. Stangl, Double-Sided Passivated Contacts for Solar Cell Applications: An Industrially Viable Approach Toward 24% Efficient Large Area Silicon Solar Cells **2019**.
- [19] S. W. Glunz, B. Steinhauser, J. I. Polzin, C. Luderer, B. Gröbel, T. Niewelt, A. M. O. M. Okasha, M. Bories, H. Nagel, K. Krieg, F. Feldmann, A. Richter, M. Bivour, M. Hermle, *Prog. Photovolt. Res. Appl.* **2021**, DOI: [10.1002/ppp.3522](https://doi.org/10.1002/ppp.3522).
- [20] Y. Lin, Z. Yang, Z. Liu, J. Zheng, M. Feng, Y. Zhi, L. Lu, M. Liao, W. Liu, D. Ma, Q. Han, H. Cheng, Q. Zeng, Z. Yuan, B. Yan, Y. Zeng, J. Ye, *Energy & Environmental Science* **2021**, 14, 6406.
- [21] A. Richter, R. Müller, J. Benick, F. Feldmann, B. Steinhauser, C. Reichel, A. Fell, M. Bivour, M. Hermle, S. W. Glunz, *Nat. Energy* **2021**, 6, 429.
- [22] D. Ma, W. Liu, M. Xiao, Z. Yang, Z. Liu, M. Liao, Q. Han, H. Cheng, H. Xing, Z. Ding, B. Yan, Y. Wang, Y. Zeng, J. Ye, *Sol. Energy* **2022**, 242, 1.
- [23] Y. Wu, G. Lucovsky, *AIP Conf. Proc.* **1998**, 449, 288.
- [24] K. Uwasawa, T. Mogami, T. Kunio, and M. Fukuma, Scaling limitations of gate oxide in p/sup +/- polysilicon gate MOS structures for sub-quarter micron CMOS devices. in Proceedings of IEEE International Electron Devices Meeting, **1993**, pp. 895.
- [25] T. Yamamoto, K. Uwasawa, T. Mogami, *IEEE Trans. Electron. Devices* **1999**, 46, 921.
- [26] M. Y. L. Jung, R. Gunawan, R. D. Braatz, E. G. Seebauer, *J. Appl. Phys.* **2004**, 95, 1134.
- [27] F. Feldmann, J. Schön, J. Niess, W. Lerch, M. Hermle, *Sol. Energy Mater. Sol. Cells* **2019**, 200, 109978.
- [28] Y. J. Oh, H.-K. Noh, K. J. Chang, *Phys. B Condens. Matter* **2012**, 407, 2989.
- [29] Y. J. Oh, J.-H. Hwang, H.-K. Noh, J. Bang, B. Ryu, K. J. Chang, *Microelectron. Eng.* **2012**, 89, 120.
- [30] S. Kim, J.-S. Park, K. J. Chang, *Nano Lett.* **2012**, 12, 5068.
- [31] D. K. Schroder, J. A. Babcock, *J. Appl. Phys.* **2003**, 94, 1.
- [32] D. L. Young, B. G. Lee, D. Fogel, W. Nemeth, V. LaSalvia, S. Theingi, M. Page, M. Young, C. Perkins, P. Stradins, *IEEE J. Photovoltaics* **2017**, 7, 1640.
- [33] M. Ghezzi, D. M. Brown, *J. Electrochem. Soc.* **1973**, 120, 146.
- [34] S.W. Jones, Diffusion in silicon. IC Knowledge LLC.
- [35] A. S. Grove, O. L. Jr, C. T. Sah, *J. Appl. Phys.* **1964**, 35, 2695.

- [36] F. A. Trumbore, *Bell Syst. Tech. J.* **1960**, 39, 205.
- [37] S. Haridoss, F. Bénérière, M. Gauneau, A. Rupert, *J. Appl. Phys.* **1980**, 51, 5833.
- [38] C. M. Lin, A. J. Steckl, T. P. Chow, *Appl. Phys. Lett.* **1988**, 52, 2049.
- [39] J. Matsuo, I. Kato, H. Horie, N. Nakayama, H. Ishikawa, *Appl. Phys. Lett.* **1987**, 51, 2037.
- [40] J. Fiedler, V. Heera, M. Voelskow, A. Mücklich, H. Reuther, W. Skorupa, G. Gobsch, M. Helm, *Acta Phys. Pol. A* **2013**, 123, 916.
- [41] T. Herrmannsdörfer, V. Heera, O. Ignatchik, M. Uhlarz, A. Mücklich, M. Posselt, H. Reuther, B. Schmidt, K. H. Heinig, W. Skorupa, M. Voelskow, C. Wündisch, R. Skrotzki, M. Helm, J. Wosnitza, *Phys. Rev. Lett.* **2009**, 102, 217003.
- [42] E. Bustarret, C. Marcenat, P. Achatz, J. Kačmarčík, F. Lévy, A. Huxley, L. Ortéga, E. Bourgeois, X. Blase, D. Débarre, J. Boulmer, *Nature* **2006**, 444, 465.
- [43] J. Margetis, D. Kohen, C. Porret, L. Lima, R. Khazaka, G. Rengo, R. Loo, J. Tolle, A. Demos, *ECS Trans.* **2019**, 93, 7.
- [44] L. Romano, A. M. Piro, E. Napolitani, G. Bisognin, A. Spada, M. G. Grimaldi, E. Rimini, *Nucl. Instrum. Methods Phys. Res., Sect. B* **2004**.
- [45] A. Casel, H. Jorke, E. Kasper, H. Kibbel, *Appl. Phys. Lett.* **1986**, 48, 922.
- [46] J. Narayan, O. W. Holland, B. R. Appleton, *J. Vacuum Sci. Technol. B Microelectr. Proc. Phenomena* **1983**, 1, 871.
- [47] C. W. White, S. R. Wilson, B. R. Appleton, F. W. Young Jr., *J. Appl. Phys.* **1980**, 51, 738.
- [48] M. Takai, S. C. Tsou, P. H. Tsien, D. Röschenhaler, H. Ryssel, *Appl. Phys. A* **1981**, 24, 319.
- [49] H. B. Harrison, S. S. Iyer, G. A. Sai-Halasz, S. A. Cohen, *Appl. Phys. Lett.* **1987**, 51, 992.
- [50] B. M. Arora, J. M. Castillo, M. B. Kurup, R. P. Sharma, *J. Electron. Mater.* **1981**, 10, 845.
- [51] P. Baeri, S. U. Campisano, G. Foti, E. Rimini, *J. Appl. Phys.* **1979**, 50, 788.
- [52] J. W. Herman, H. E. Elsayed-Ali, *Phys. Rev. Lett.* **1992**, 69, 1228.
- [53] T. Hoshikawa, X. Huang, S. Uda, T. Taishi, *J. Cryst. Growth* **2006**, 290, 338.
- [54] F. Stevie, *Secondary Ion Mass Spectrometry: Applications for Depth Profiling and Surface Characterization*, Momentum Press, LLC, New York **2015**.
- [55] K. B. Joelsson, Y. Fu, W.-X. Ni, G. V. Hansson, *J. Appl. Phys.* **1997**, 81, 1264.
- [56] F. Szmulowicz, *Phys. Rev. B* **1986**, 34, 4031.
- [57] G. Impellizzeri, E. Napolitani, S. Boninelli, V. Privitera, T. Clarysse, W. Vandervorst, F. Priolo, *Appl. Phys. Express* **2012**, 5, 1301.
- [58] C. Hollemann, F. Haase, M. Rienäcker, V. Barnscheidt, J. Krügener, N. Folchert, R. Brendel, S. Richter, S. Großer, E. Sauter, J. Hübner, M. Oestreich, R. Peibst, *Sci. Rep.* **2020**, 10, 658.
- [59] B. Nemeth, D. L. Young, M. R. Page, V. LaSalvia, S. Johnston, R. Reedy, P. Stradins, *J. Mater. Res.* **2016**, 31, 671.
- [60] G. Masetti, M. Severi, S. Solmi, *IEEE Transactions on Electron Devices* **1983**, 30, 764.
- [61] L. Romano, A. Piro, M. Grimaldi, G. Bisognin, E. Napolitani, D. De Salvador, *Phys. Rev. Lett.* **2006**, 97, 136605.
- [62] R. Skrotzki, J. Fiedler, T. Herrmannsdörfer, V. Heera, M. Voelskow, A. Mücklich, B. Schmidt, W. Skorupa, G. Gobsch, M. Helm, J. Wosnitza, *Appl. Phys. Lett.* **2010**, 97, 192505.
- [63] J. Fiedler, V. Heera, R. Hübner, M. Voelskow, S. Germer, B. Schmidt, W. Skorupa, *J. Appl. Phys.* **2014**, 116, 24502.
- [64] T. Sadi, C. Medina-Bailon, M. Nedjalkov, J. Lee, O. Badami, S. Berrada, H. Carrillo-Nunez, V. Georgiev, S. Selberherr, A. Asenov, *Materials (Basel)* **2019**, 12, 124.
- [65] N. Sclar, *Phys. Rev.* **1956**, 104, 1559.
- [66] A. S. Kale, W. Nemeth, S. P. Harvey, M. Page, D. L. Young, S. Agarwal, P. Stradins, *Sol. Energy Mater. Sol. Cells* **2018**, 185, 270.
- [67] H. Berger, Contact resistance on diffused resistors. in 1969 IEEE International Solid-State Circuits Conference. Digest of Technical Papers. **1969**, vol. XII, pp. 160.
- [68] W. Wang, H. Lin, Z. Yang, Z. Wang, J. Wang, L. Zhang, M. Liao, Y. Zeng, P. Gao, B. Yan, J. Ye, *IEEE J. Photovoltaics* **2019**, 9, 1113.
- [69] M. W. Denhoff, *J. Phys. D Appl. Phys.* **2006**, 39, 1761.
- [70] W. Kern, *J. Electrochem. Soc.* **1990**, 137, 1887.
- [71] K. Reinhardt, W. Kern, *Handbook of Silicon Wafer Cleaning Technology*, 2nd ed, Norwich, NY, USA **2008**.
- [72] Interactions of ions with matter – the Stopping and Range of Ions in Matter. James. F. Ziegler. <http://www.srim.org> (accessed).
- [73] D. E. Hoglund, M. O. Thompson, M. J. Aziz, *Phys. Rev. B* **1998**, 58, 189.
- [74] B. Hallam, B. Tjahjono, T. Trupke, S. Wenham, *J. Appl. Phys.* **2014**, 115, 44901.
- [75] D. E. Kane and R. Swanson, Measurement of the emitter saturation current by a contactless photoconductivity decay method. **1985**.
- [76] R. A. Sinton, A. Cuevas, and M. Stuckings, Quasi-steady-state photoconductance, a new method for solar cell material and device characterization. in Conference Record of the Twenty Fifth IEEE Photovoltaic Specialists Conference – 1996, **1996**, 457.
- [77] A. Cuevas, R. A. Sinton, *Prog. Photovolt. Res. Appl.* **1997**, 5, 79.
- [78] A. Richter, S. W. Glunz, F. Werner, J. Schmidt, A. Cuevas, *Phys. Rev. B* **2012**, 86, 165202.
- [79] L. A. Giannuzzi, F. A. Stevie, *Micron* **1999** 30, 197.
- [80] S. Kalinin, A. Gruverman, *Scanning Probe Microscopy: Electrical and Electromechanical Phenomena at the Nanoscale*, Springer Science & Business Media, New York, **2007**.